Laser-Driven Microsecond Temperature Cycles Analyzed by Fluorescence Polarization Microscopy

Rob Zondervan, Florian Kulzer, Harmen van der Meer, Jos A. J. M. Disselhorst, and Michel Orrit
Molecular Nano-Optics and Spins, Huygens Laboratory, Leiden Institute of Physics, 2333 CA Leiden, The Netherlands

ABSTRACT We demonstrate a novel technique to achieve fast thermal cycles of a small sample (a few femtoliters). Modulating a continuous near-infrared laser focused on a metal film, we can drive the local temperature from 130 to 300 K and back, within a few microseconds. By fluorescence microscopy of dyes in a thin glycerol film, we record images of the hot spot, calibrate its temperature, and follow its variations in real time. The temperature dependence of fluorescence anisotropy, due to photophysics and rotational diffusion, gives a steady-state temperature calibration between 200 and 350 K. From 200 to 220 K, we monitor temperature more accurately by fluorescence autocorrelation, a probe for rotational diffusion. Time-resolved measurements of fluorescence anisotropy give heating and cooling times of a few microseconds, short enough to supercool pure water. We designed our method to repeatedly cycle a single (bio)molecule between ambient and cryostat temperatures with microsecond time resolution. Successive measurements of a structurally relevant variable will decompose a dynamical process into structural snapshots. Such temperature-cycle experiments, which combine a high time resolution with long observation times, can thus be expected to yield new insights into complex processes such as protein folding.

INTRODUCTION

Temperature jumps of a few Kelvin induced by nanosecond to picosecond laser pulses are a well-established method to unfold DNA, RNA, polypeptides, or proteins at room temperature (1–10). In these experiments fast heating is obtained by dumping a large amount of optical energy into the sample. The subsequent cooling is slow, because cooling entirely relies on heat diffusion out of a rather large volume. Because active optical cooling is impossible, we propose to speed up cooling by dramatically reducing the sample volume, in a modified temperature-jump scheme. Placing our sample in a cold cryostat, we heat a small volume up to room temperature with a continuous-wave laser focused on an absorbing metal film. The moment the heating laser is switched off, the heated volume quickly reverts to the cryostat temperature. In this way, we can repeatedly cycle the temperature between a low and a high value, as schematically presented (see Fig. 1). With a diffraction-limited hot spot ~ 1 μm in size, the expected heating and cooling times are on the order of a microsecond.

Fast thermal cycles attractively dovetail with single-molecule observations. Indeed, although fast cooling requires a huge temperature gradient, a single biomolecule can always be placed at the center of the focal spot, where the gradient vanishes. In contrast to this, temperature inhomogeneity would seriously degrade traditional ensemble measurements. Once properly characterized and calibrated, our method will be applicable to fast processes at room temperature. Optically probing successive series of snapshot structures of the same freeze-quenched single molecule would open the way to reconstruction of its folding and reaction pathways.

This work demonstrates and characterizes the proposed temperature cycles between 130 K and ambient temperature. To obtain such large temperature variations, one cannot rely on absorption by the sample medium (which should be of optical quality). Previous studies of heating effects in intense laser fields, for instance in multiphoton spectroscopy (11,12) or in optical traps (13–15), in optically clear samples and for practical powers, have achieved temperature rises of a few Kelvin at most. We therefore decided to place our sample in contact with an efficient absorber of near-infrared (NIR) radiation, in our case a thin metal layer on a glass substrate.

To determine the efficiency of the laser-induced local heating, we optically measure the spatial temperature profile of the hot spot, and the kinetics of heating and cooling. We have tried Raman scattering from poly-(methylmethacrylate) coverslides, coated by an absorbing metal film. This technique probes the local temperature rather accurately (up to ± 1 K), but requires minutes of acquisition (R. Zondervan, unpublished data). Translational and rotational diffusion of fluorophores are two optically accessible quantities depending on temperature. This dependence can be extended to a broader temperature range in glassy and supercooled liquid matrixes such as glycerol, in which the viscosity varies by several orders of magnitude between 200 and 300 K (16–19). Translational diffusion is often measured by fluorescence correlation spectroscopy (FCS), which has the disadvantage that the observed diffusion time depends on the effective focal volume (20,21). Rotational diffusion is a more convenient probe of local temperature, because it only depends on intrinsic parameters. It leads to a reduction of the steady-state fluorescence anisotropy when the rotation time approaches

Submitted September 27, 2005, and accepted for publication December 28, 2005.

Address reprint requests to Michel Orrit, E-mail: orrit@molphys.leidenuniv.nl.

0006-3495/06/04/2958/12 $2.00

doi: 10.1529/biophysj.105.075168

the fluorescence lifetime (22). At lower temperatures and low fluorophore concentration, rotational diffusion of the emitters induces observable fluctuations in fluorescence polarization. The fluctuations of the anisotropy around its average steady-state value are characterized by a rotation correlation time, deduced from autocorrelation functions (23–25). We will refer to this FCS-like method as fluorescence anisotropy correlation spectroscopy (FACS). The main difference between the two methods is the normalization of anisotropy to the total intensity, which makes FACS much less sensitive than FCS to photoblinking and other non-orientational fluctuations.

Here, we describe a setup that combines the proposed temperature cycles with low-temperature fluorescence microscopy. The required laser-induced local heating is visualized and characterized at a cryostat temperature of 130 K by fluorescence and fluorescence anisotropy imaging experiments in a rhodamine 6G (R6G) solution in glycerol deposited on an absorbing substrate. The fluorescence (anisotropy) of R6G in glycerol is mainly a probe of rotational diffusion, but is also affected by photoblinking. This leads to a continuous change of steady-state anisotropy with temperature above 200 K. A more accurate temperature calibration between 200 and 220 K is provided by FACS measurements on perylenedicarboximide (PDI) in glycerol. Finally, the heating and cooling kinetics in the center of the laser-induced hot spot are studied in real time by the fast responses of both the fluorescence intensity and the fluorescence anisotropy of R6G in glycerol.

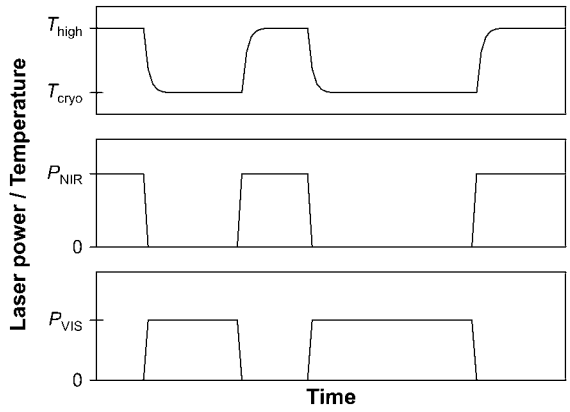

FIGURE 1 Scheme of the proposed thermal cycles between cryogenic and room temperatures. A focused near-infrared laser beam with power P_{NIR} (*middle graph*) rapidly raises the local focus temperature to T_{high} (*top graph*). The moment the NIR laser is switched off, the temperature quickly drops back to the surrounding temperature T_{cryo}. In future experiments, a visible laser (*bottom graph*) with power P_{VIS} will excite fluorescent labels during the cold periods at T_{cryo} only.

EXPERIMENTAL SECTION

The setup, schematically shown in Figs. 2 and 3, combines a low-temperature fluorescence microscope with single-molecule sensitivity and a heating path for the fast temperature cycles. The sample, a fluorophore-doped glycerol film spin-coated on an absorbing metal film, is mounted in a cryostat (SVT-200-5; Janis, Wilmington, MA). Fig. 2 shows the configuration of the sample plate in the cryostat with the two separate optical pathways for probing and heating. Optical paths inside and outside the cryostat are described separately hereafter.

The probing beam (514.5 nm) (see Fig. 2) enters the cryostat through its bottom window and is focused by a custom-made low-temperature microscope objective (NA = 0.85) onto the sample. The NIR heating beam (785 nm) enters the cryostat through one of its side windows, is directed downward by a 45° mirror and focused by an aspheric singlet lens (NA = 0.68). This 4π-like geometry was chosen to prevent photobleaching of the sample, which could be caused by two-photon excitation by the NIR laser during possibly extended heating periods. The sample plate and the NIR lens (together with the 45° mirror) are separately held by a homebuilt cryostat insert (cf. Fig. 4). This insert facilitates the adjustment of both elements in three dimensions so that the visible and NIR foci can be overlapped on the same sample position.

The part outside the cryostat comprises two separate optical ''subsetups'' that handle the optical probing (514.5 nm) and the NIR heating (785 nm). The probing part (cf. Fig. 3, *left* of the cryostat) is a laser-scanning confocal microscope and takes care of the excitation and subsequent, polarization-dependent, detection of fluorescence. The heating part (cf. Fig. 3, *right* of the cryostat) is also a laser-scanning confocal microscope but without detection path. An acousto-optical modulator (AOM) (AA Opto-Electronic, Orsay, France) is placed in the NIR beam to allow modulation and fast switching of the heating laser. In the next subsection, we describe in more detail the configuration inside the cryostat, i.e., the homebuilt cryostat insert, the absorbing sample plate, and the custom-made low-temperature microscope objective. In the remaining two subsections we dwell on the optics outside the cryostat and the preparation of water-free fluorophore-doped glycerol films.

Inside the cryostat

The core of the setup (cf. Fig. 2) is placed in a five-window variable-temperature cryostat (SVT-200-5; Janis) with active temperature stabilization

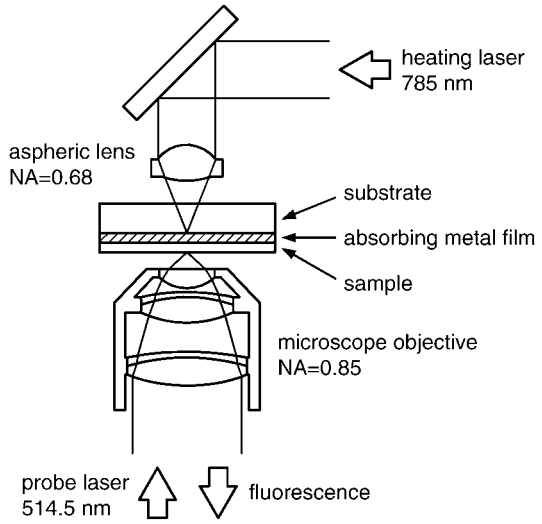

FIGURE 2 Scheme of the optical paths around the sample plate in the cryostat. The sample plate is a glass substrate (thickness 0.17 mm), coated with a thin, absorbing metal film (thickness 50 nm), itself covered with the fluorescent solution layer. Fluorescence is excited (514.5 nm) and collected by the custom-made 10-lens objective (NA = 0.85, represented here by a simplified five-lens scheme) beneath the sample. Above it, a mirror at 45° and an aspheric singlet lens (NA = 0.68) direct and focus the NIR beam (785 nm) onto the metal film right across the visible focus.

(32B; CryoCon, Rancho Santa Fe, CA). The homebuilt cryostat insert consists of two parts: the objective holder at the bottom and the sample holder, the long top part that also carries the NIR lens. Fig. 4 shows a detailed drawing of the lower third of the cryostat insert.

The objective holder is spring loaded against the cryostat's bottom and remains in the cryostat upon sample change. It holds a 10-lens microscope objective (NA = 0.85, 60 times) which we specially developed for repetitive operation at cryogenic temperatures in cooperation with the company Bernhard Halle Nachfl. (Berlin, Germany). This custom-made objective replaces commercially available five-lens objectives, which often survive only a few cycles between room and low temperatures. Its antireflection coated lenses are made from glasses selected for their low thermal expansion and resistance to moisture. The lenses, mounted without any glue or cement, are held in place by spacer rings in a titanium housing. Longitudinal slits are cut in this housing to enable thermal expansion during thermal cycles. The objective is infinity corrected and generates diffraction-limited excitation spots. Imaging fluorescent beads (20 nm Nile Red soaked latex beads; Molecular Probes, Eugene, OR) with 514.5-nm excitation, we found an average spot size of ~450 nm over the whole range from 4 to 295 K. For the five-lens alternative, the spot size was 600 nm, and the average collected intensity was two to three times lower.

The sample holder is coupled kinematically to the objective holder by three self-locking prongs (cf. Fig. 4). The sample plate at the lower end (see Fig. 2) is a standard 20-mm round coverslide (thickness 0.17 mm) coated with a thin (50 nm) sputtered metal layer. We chose thin films because the residual NIR transmission helps alignment and reduces heat conduction by the metal. In the course of this work, we use either homemade nickel-chromium films or custom-made chromium films (Berliner Glas, Berlin, Germany). The absorption of metal films strongly depends on preparation (26). Our NiCr films absorb ~30–40% and transmit 2% at 785 nm. The chemically inert Cr films absorb roughly 10–15% and transmit ~1%. The Cr films can be optionally coated with a thin (50 nm) silica layer to reduce quenching by isolating the fluorophores from the metal.

On the sample mount, close to the sample plate, a silicon diode (Lakeshore, Westerville, OH) measures the actual cryostat temperature around the sample. The sample mount can be moved in three dimensions by piezo-driven inchworm motors (Attocube Systems, Munich, Germany) (see Fig. 4). The ''axial'' piezo motor shifts the sample vertically into the focus of the microscope objective. The other two piezo motors command an area of 5×5 mm^2 in the sample plane. The NIR heating beam is reflected down by a mirror onto a singlet lens with NA 0.68 (350330-B; Thorlabs, Karlsfeld, Germany). The mirror and the lens are mounted together above the sample (cf. Figs. 2 and 4). This assembly can also be positioned in three dimensions. A fourth piezo motor shifts the lens vertically to bring its focus at the metal-glass interface (cf. Fig. 2). With two mechanical controls, we can position the lens-mirror assembly with micrometer precision in the (x,y) focal plane (cf. Fig. 4). These controls actuate two spring-loaded flexure hinges, which are elastically deformable bridges thinned out in one metal piece. When slightly tilted around either hinge, the lens-mirror holder also shifts in the sample plane. Our group has previously shown that flexure hinges provide reliable and stable positioning in low-temperature microscopy (27,28).

Outside the cryostat

The probing part of the setup is the laser-scanning confocal microscope shown in Fig. 3. The automated beam scanner is based on two one-axis scan mirrors (Cambridge Technology, Cambridge, MA, 6450 galvanometer

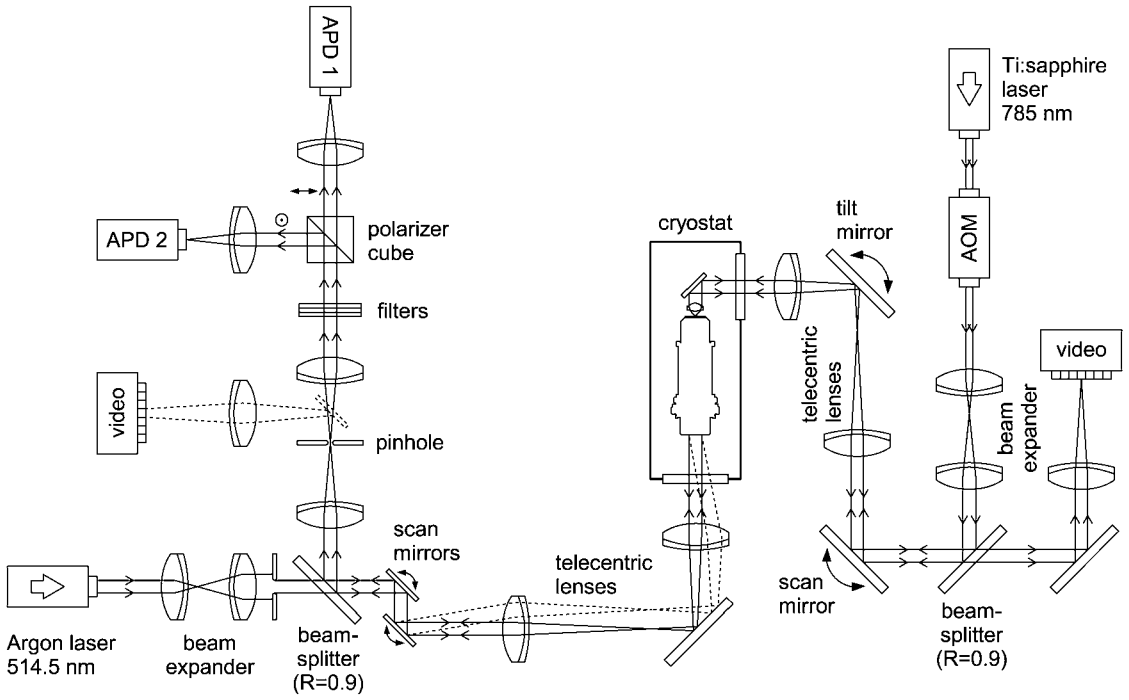

FIGURE 3 Schematic layout of the temperature-cycle setup. The two optical pathways, for probing (514.5 nm) and heating (785 nm), are completely separated. The probing part, represented to the left of the cryostat, is a laser-scanning confocal microscope with single-molecule sensitivity. The automatized laser scanner is composed of two one-axis galvanometer scan mirrors. The excitation and detection paths are separated by a (90/10) beam splitter. Besides standard components (beam expander, telecentric system, spatial filter, and spectral filters) the microscope includes a video camera to facilitate the positioning of the sample into the focal plane of the microscope objective. Collected fluorescence photons are sorted out by a polarizer cube and sent to two independent detectors for the parallel and perpendicular polarizations. The NIR (785 nm) optical path (*right* of the cryostat) corresponds to the excitation path only of a laser-scanning confocal microscope. A second video camera monitors the focus of the NIR beam on the sample. An acousto-optical modulator rapidly switches the NIR power. Fig. 2 shows a detail of the optical components inside the cryostat.

optical scanner). The excitation and detection paths are separated by a (90/10), (reflection/transmission), beam splitter (AHF Analysentechnik, Tübingen, Germany). The excitation source, a multiline argon-ion laser (Stabilite 2017; Spectra-Physics, Mountain View, CA), pumps the NIR laser with 90% of its output. The remaining 10% are dispersed in a Pellin-Broca prism (Bernhard Halle, Berlin, Germany), and the 514.5-nm line is selected for excitation. This beam passes a variable attenuator (M925B; Newport, Irvine, CA), a laser-line clean-up filter (LCS10-515-F; Laser Components, Hudson, NH), a combination of a beam expander and a diaphragm to optimize the illumination of the microscope objective (cf. Fig. 3), and reaches the beam splitter.

Starting from the beam splitter, the detection path (cf. Fig. 3) includes a spatial filter (two lenses and a 100-μm pinhole). A flip mirror can be inserted between the pinhole and the second lens for imaging by a color video camera (Ganz, London, UK), which helps us bring the sample at the focal plane of the microscope objective. After the spatial filter, two notch filters (HNPF-514.5 and HSPF-785.0; Kaiser Optical Systems, Ann Arbor, MI), centered at 514.5 and 785 nm, respectively, and two long-pass filters (AHF Analysentechnik HQ525LP and HQ530LP) remove residual laser light. Fluorescence photons are then polarization-selected by a polarizer cube (33 5641; Linos, Göttingen, Germany) and detected by two avalanche photodiodes (SPCM-AQR; Perkin-Elmer, Foster City, CA). The setup and data acquisition are computer controlled with an AdWin-Gold system (Keithley Instruments, Cleveland, OH) and software written in LabVIEW 6.1 (National Instruments, Austin, TX).

The heating source (Fig. 3) at 785 nm is a broadband Ti:Sa laser (Spectra-Physics 3900S), pumped by the argon-ion laser. The intensity at the sample can reach 75 mW in our current configuration. The laser beam can be quickly switched on and off by an acousto-optical modulator (AA Opto-Electronic; see Fig. 3). It passes a beam expander, a (90/10) beam splitter (AHF Analysentechnik), and is directed to the cryostat side window by a telescope consisting of two mirrors and two lenses (cf. Fig. 3). The bottom mirror acts as a manual scan mirror and the top mirror can be tilted for further optimization. The NIR focus on the metal film is monitored by a color video camera (Ganz) that receives 10% of the back-reflected NIR light.

Sample preparation

The samples are either 10^{-5} M rhodamine 6G (R6G) or 10^{-7} M PDI solutions in glycerol with 6–8% water. The glycerol solution is directly spin-coated at 6000 rpm on the metal-coated glass slip. To ensure the stability of the liquid film, we found it important to thoroughly clean and oxidize the metal surface just before spin-coating. This was done in an ultraviolet-ozone cleaner (model 42-220; Jelight, Irvine, CA). We estimate the film thickness to be 1–3 μm. Because the viscosity of glycerol changes dramatically with water content (16,17), we keep the films under a dry and inert helium atmosphere throughout all experiments. Before cooling, the samples are dried at room temperature in the cryostat by repeated pumping and flushing with helium. Fluorescence anisotropy critically depends on viscosity. Our measurements show that the water content of glycerol is $<1\%$, i.e., too low to practically distinguish the solution from pure glycerol under our experimental conditions.

RESULTS AND DISCUSSION

We first briefly discuss the physical properties of glycerol. Because each molecule has three OH groups, glycerol forms a complex, highly branched network of intermolecular hydrogen bonds. At room temperature, the liquid has a viscosity 1000 times higher than that of water (16,17). Although it can be crystallized, glycerol's high viscosity usually leads to supercooling at lower temperatures, and to a glass transition at $\sim$190 K (18,19,29). Between room temperature and the glass transition, the viscosity increases by 10 orders of magnitude! This makes viscosity an extremely sensitive temperature probe (18,19). The exact temperature dependence of the viscosity η of glycerol can be approximated by a Vogel-Fulcher-Tammann-Hesse (VFTH) law (18,30–32):

$$\eta = \eta_0 10^{\left(\frac{B}{T-T_0}\right)}, \tag{1}$$

with below 283 K, $\eta_0 = 7.9 \times 10^{-8}$ Pa s, $B = 1260$ K, $T_0 = 118$ K, and above 283 K, $\eta_0 = 3.54 \times 10^{-6}$ Pa s, $B = 780$ K, $T_0 = 153$ K (18).

In this work, we visualize the temperature dependence of the viscosity through the rotation of fluorescent molecules in glycerol. Supposing the fluorophores rotate isotropically, we have the following expression for the rotation correlation time τ_R (22):

$$\tau_R = \frac{V\eta}{k_B T}, \tag{2}$$

with V the hydrodynamic molecular volume, 0.419 nm^3 for rhodamine 610 (a molecule quite similar to R6G) (33), and k_B the Boltzmann constant. The ''rotation'' curve in Fig. 5 shows the expected rotation correlation time of a typical organic fluorophore (rhodamine 610) in glycerol between 190 and 360 K based on Eqs. 1 and 2.

The rotation correlation time of a fluorophore can be measured through the steady-state fluorescence anisotropy r, when this time is on the order of the fluorescence lifetime (22). The anisotropy is the normalized difference between the signal from the parallel (to excitation) $F_\parallel$ and that from the perpendicular detection channel $F_\perp$ and is defined as follows:

$$r = \frac{F_\parallel - F_\perp}{F_\parallel + 2F_\perp}. \tag{3}$$

The anisotropy decreases from its maximum value r_0 with decreasing rotation correlation time (and thereby with increasing temperature) according to Perrin's law (22):

$$\frac{1}{r} = \frac{1}{r_0}\left(1 + \frac{\tau_F}{\tau_R}\right) = \frac{1}{r_0}\left(1 + \frac{k_B \tau_F}{V\eta} T\right), \tag{4}$$

with τ_F the fluorescence lifetime, 4×10^{-9} s for R6G (34). In practice this decrease is only measurable at temperatures where the rotation time is not larger than $\sim$100 times the fluorescence lifetime, i.e., at temperatures higher than 280 K for a small organic dye in glycerol (cf. Fig. 5). Steady-state fluorescence anisotropy of an ensemble is easy to measure within milliseconds. Scanning the confocal volume provides a temperature map with high spatial resolution in a reasonable time.

The temporal fluctuations of fluorescence anisotropy in a small volume can also be correlated (fluorescence anisotropy correlation spectroscopy), if the fluorophore concentration is not too high. A characteristic rotation correlation time τ_R may be obtained by adjusting a single exponential to the autocorrelation function $C_r'(t)$ of the time trace of anisotropy (23,24):

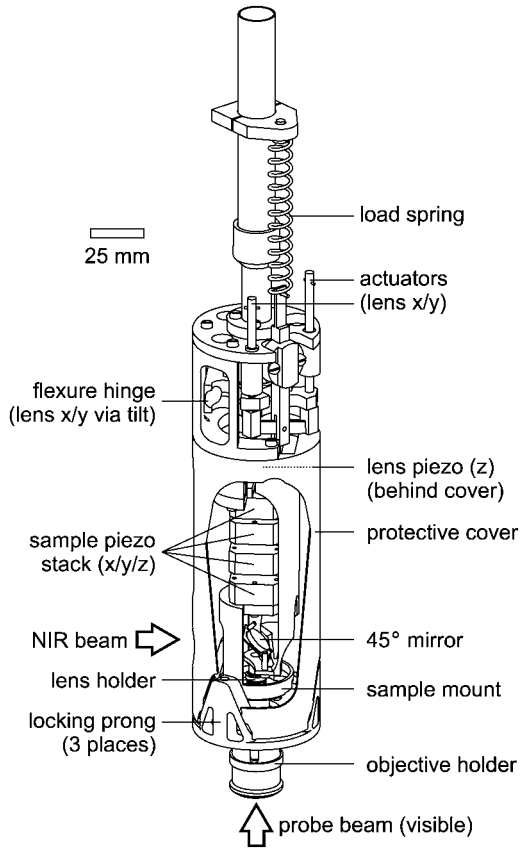

FIGURE 4 Simplified drawing of the bottom of the homebuilt cryostat insert. The protective cover is ''cut open'' to show the internal part and the optical elements schematized in Fig. 2. Sample holder and objective holder are separate parts, self-locked to one another by three prongs (one of them is labeled). A piezo stack moves the sample mount in three dimensions (x, y, z of sample), and a fourth piezo actuator moves the lens-mirror assembly to focus the NIR laser onto the sample (z of lens). Additionally, two mechanical actuators coarsely control the lens-mirror assembly (x, y of lens). This mechanical movement is a backlash-free bending of two spring-loaded flexure hinges.

$$C_r'(t) = \frac{\langle r(t'+t)r(t')\rangle}{\langle r(t')\rangle^2} - 1 \propto \exp\left(-\frac{t}{\tau_R}\right). \quad (5)$$

The temperature window of this method is limited to the range 200–240 K. At higher temperatures the rotation times are so short (<100 μs; see Fig. 5) that the number of photons detected in the rotation time is too low. At temperature lower than 200 K, the rotation gets so slow that bleaching starts to limit the observation time (overcoming the detector's dark counts requires a minimum excitation intensity). The time averaging required to sample enough rotation events (at least 10 times the rotation correlation time) makes the method too slow for temperature imaging.

Fluorophores not only rotate, they also spatially diffuse. Although we do not use translational diffusion as a temperature probe, it becomes important at high heating powers and may affect our results. The translational diffusion constant D (20):

$$D = \frac{k_B T}{6\pi\eta R}, \quad (6)$$

depends on R the hydrodynamic molecular radius, 0.464 nm for rhodamine 610 (33). A characteristic diffusion time is fixed by the volume through which a molecule diffuses, i.e., the focal volume in FCS. For three-dimensional isotropic diffusion, the translation correlation time τ_T is approximately:

$$\tau_T = \frac{a^2}{6D}, \quad (7)$$

with a the size of the spot through which the molecule diffuses. For a typical laser spot size, $a = 1$ μm, we obtain the ''translation'' (*top*) curve in Fig. 5. It shows that below 240 K, translation may be neglected on the timescale of our experiments, several minutes.

Temperature calibration of the steady-state fluorescence anisotropy

Fig. 6 *a* shows the variations with temperature of the steady-state fluorescence anisotropy of 10^{-5} M R6G in glycerol. We will use this curve to determine the steady-state temperature in the center of the laser-heated spot. Each point is generated by taking the average anisotropy value of a complete 20×20 μm^2 image. To be completely consistent with images presented later, we use the same experimental conditions, excitation intensity (50 W/cm^2), scanning step (200 nm), and acquisition time (10 ms/point). Under our specific experimental conditions, the anisotropy signal is independent of

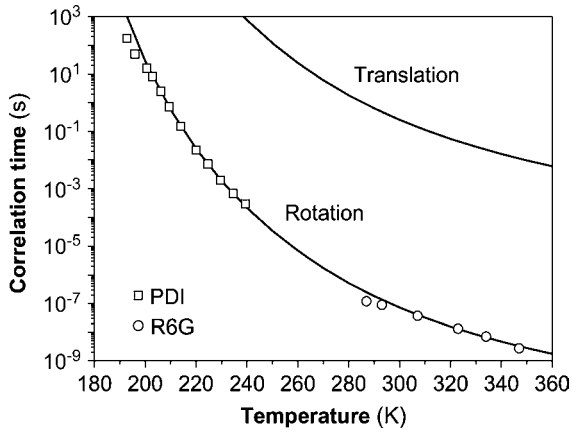

FIGURE 5 (*Solid lines*) Calculated temperature dependence of the rotation (*bottom curve*) and translation (*top curve*) correlation times for rhodamine 610 in glycerol. For translational diffusion, the spot size a (cf. Eq. 7) is chosen equal to 1 μm. The rotation curve is compared to experimental results obtained in this work. The circles stem from steady-state fluorescence anisotropy measurements on R6G in glycerol. The squares represent FACS measurements on PDI in glycerol, which will be presented in more detail elsewhere (R. Zondervan, J. Berkhout, F. Kulzer, and M. Orrit, unpublished data). Both data sets are in good agreement with the model curve.

temperature below 200 K. Between 200 and 280 K it increases from 0.18 to ~0.27, then rapidly decreases again to 0.11 at 345 K.

Between 200 and 280 K, glycerol is too viscous for significant reorientation of the dye during its fluorescence lifetime. We attribute the observed variation of the anisotropy to reversible photoinduced processes called photoblinking, causing the typical flickering of single-molecule signals. This is confirmed by behavior similar to that seen in Zondervan et al. (35) for R6G in poly(vinyl-alcohol), i.e., sublinear dependence of fluorescence with excitation intensities, and recovery of the fluorescence signal in the dark after illumination. This recovery is accompanied by that of the anisotropy. As discussed in Zondervan et al. (35), saturation at intensities as low as 50 W/cm^2 cannot be due to intersystem crossing alone. Here, too, we attribute it to electron transfer from glycerol to the excited rhodamine, leading to the radical anion of R6G, a long-lived dark state. Being excitation dependent, photoblinking influences fluorescence anisotropy. If a molecule's transition dipole lies along the laser field, it will be excited more often and will have a larger probability to convert to the dark state. The ratio of $F_{\parallel}/F_{\perp}$ thus decreases, leading to a weaker apparent anisotropy. Thermally activated recovery from the dark state, previously observed for R6G in poly(vinyl-alcohol) (35), reduces the discrepancy when the temperature increases from 200 to 280 K (*dashed straight line* in Fig. 6 *a*). Below 200 K tunneling dominates activation (35), and the apparent anisotropy becomes independent of temperature.

Above 280 K, the anisotropy closely follows Perrin's equation (4) as the rotation time quickly shortens and becomes comparable to the fluorescence lifetime. Due to the interplay of photoblinking and rotational diffusion, we cannot reliably measure the maximum fluorescence anisotropy r_0 of R6G in glycerol. Although the theoretical maximum r_0 of anisotropy in a rigid medium is 0.40, this value is only observed for purely electronic S_0–S_1 transitions, where the emission and absorption dipole moments are the same. Vibronic components in emission and absorption may possess dipole moments with different orientations with respect to the molecular axes (e.g., parallel or perpendicular to the axis in the case of a molecule with C_2 symmetry). This effect, which is often represented by an average angle $\overline{\alpha}$ between excitation and emission moments, leads to a reduced r_0 (22):

$$r_0 = \frac{2}{5}\frac{3\overline{\cos^2\alpha} - 1}{2}. \quad (8)$$

In the (ionic) rhodamine dyes, this effect yields a value of $\overline{\alpha} \sim 30°$ (33), and a value of 0.25 for r_0. We have measured r_0 for R6G in the rigid polymer poly(vinyl-alcohol) (36–38) at room temperature (sample preparation described elsewhere (35)). Our experimental conditions (confocal scan with step size 1 μm, acquisition time 10 ms/point, and excitation intensity 30 W/cm^2) were chosen such that photoblinking is negligible (35). We find $r_0 = 0.28$, in good agreement with the above value from literature (0.25). We obtain the solid line in Fig. 6 *a* by inserting $r_0 = 0.28$ and the temperature dependence (Eq. 1) of the viscosity η in Eq. 4, and find an excellent agreement with experimental results from 280 to 350 K. The deduced rotation correlation times appear as the circles in Fig. 5. The sudden disappearance of photoblinking effects at temperatures higher than 280 K can be ascribed to an even more efficient recovery process from the dark state, the diffusion and recombination of the geminate ions.

Imaging the laser-induced hot spot

We image the laser-induced hot spot with either total fluorescence ($F_{\parallel} + F_{\perp}$) or fluorescence anisotropy (Eq. 3). We use the latter images to determine the temperature in the center of the hot spot as a function of heating power. The cryostat temperature is 130 K, the visible excitation intensity 50 W/cm^2, the image size 20 × 20 μm^2, the step size 200 nm, and the acquisition time 10 ms/point. The NIR laser is applied continuously during each scan, and its power is varied from 0 up to 10 mW by steps of ~0.4 mW.

Fig. 7 shows confocal images of the total fluorescence of 10^{-5} M R6G in glycerol with NIR laser powers of either 0, 5.0, or 8.5 mW applied at a fixed position. At 0 mW (cf. Fig. 7, *a* and *b*) the image is uniformly bright, as expected for a fairly concentrated sample. The image recorded at 5 mW NIR power (cf. Fig. 7, *c* and *d*) shows a bright spot at the heating location with a maximum intensity twice that at 130 K and a full width at half-maximum (FWHM) of ~4 μm. This fluorescence increase is caused by the activated recovery from the dark state (cf. previous subsection). At higher heating power, the hot spot turns darker and is surrounded by a bright ring (cf. Fig. 7, *e* and *f*). This ring is found to be persistent. It is formed when R6G molecules start to translationally diffuse over the time- and lengthscales of the experiment. The strong temperature gradient around the heated spot induces a diffusion-time gradient (short time at the center, long at the surroundings), which traps the molecules at the colder edge and depopulates the center. The moment the heating abruptly ceases, the molecules are stuck, making the ring a permanent feature. A diffusion distance of 2 μm within a heating time of 50 s (half the scan time), allows us to estimate an average temperature of 270 K over the diffusion area (Fig. 5). The maximum temperature in the center must be somewhat higher, but cannot be determined accurately in this way.

From the same data used for Fig. 7, we calculate the steady-state fluorescence anisotropy images (cf. Eq. 3) shown in Fig. 8. At 0 mW (cf. Fig. 8, *a* and *b*), anisotropy is uniform. Heating first increases the anisotropy (cf. Fig. 8, *c* and *d*), again due to photoblinking. At still higher power (cf. Fig. 8, *e* and *f*) a high-anisotropy ring is formed, whereas the anisotropy in the center drops below its initial value (compare Fig. 8, *b* and *f*). This image agrees with the temperature calibration of Fig. 6 *a*, with an initial increase between 200

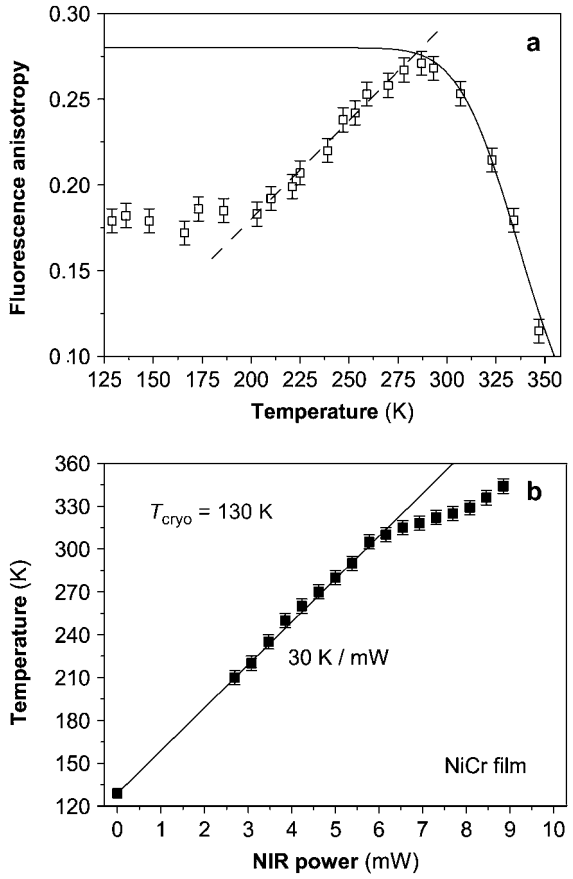

FIGURE 6 (*a*) Variations of the fluorescence anisotropy of R6G in glycerol with temperature. The anisotropy values have been averaged over a 20×20 μm^2 image (visible laser intensity 50 W/cm^2, step size 200 nm, acquisition time 10 ms/point). The solid line is the expected dependence of the steady-state anisotropy due to rotational diffusion; see Eq. 4. The dashed line guides the eye through a variation mainly due to photoblinking (see text). The error bars are 95% confidence intervals ($\pm 2\sigma = \pm 0.007$). (*b*) Actual temperature calibration with anisotropy in the center of the heating spot, as a function of heating power. The temperature first scales linearly with applied power with a slope of 30 K/mW (*solid line*). The deviation above 300 K is probably due to coupled matter and heat transport out of the heated spot when glycerol becomes very fluid. The accuracy of the calibration is ± 5 K, indicated by error bars.

and 280 K and a decrease above 280 K due to rotational diffusion. Note that this ring has a completely different origin from that of Fig. 7 *e*, because the anisotropy is normalized to total intensity (cf. Eq. 3). Indeed, it utterly disappears as soon as heating is switched off.

The center temperature is calibrated from the fluorescence anisotropy as a function of NIR power in a series of images at varying NIR power. The corresponding temperatures follow from Fig. 6 *a*, first from the dashed line (photoblinking) as long as the anisotropy increases, then from the solid curve (rotation) when it starts to decrease. The resulting local-temperature calibration is shown in Fig. 6 *b*. The images in Fig. 8, *c* and *e*, yield two points in that calibration curve. The accuracy ($\pm 2\sigma$) of the points in Fig. 6 *b* is $\sim \pm 5$ K. The local temperature is found to vary linearly with the NIR power until 310 K. The slope is 30 K/mW for the NiCr film (Fig. 6 *b*). Around 310 K the heating suddenly becomes less efficient. Because the thermal transport properties of glycerol and BK 7 glass do not significantly vary around this temperature (29,39), we attribute the change to convective transport. We indeed have observed that the glycerol film breaks and irreversibly retracts from the heating location at a NIR heating power of $\sim$10 mW (data not shown).

The FWHM of the feature at 5 mW NIR power (cf. Fig. 8 *c*) is ~ 5 μm and the temperature in the center 280 K. This corresponds to a maximum temperature gradient of ~ 50 K/μm. Accordingly, we expect the heating and cooling times to be in the microsecond domain. In the subsection ''Kinetics of heating and cooling'', we directly probe the heating and cooling kinetics with time-resolved fluorescence intensity and anisotropy measurements.

Steady-state local temperature from anisotropy correlation

At temperatures below 240 K, the rotational diffusion of fluorophores in glycerol becomes slow enough to allow rotation-time determination by FACS. To reduce interference from photoblinking fluctuations, we replaced R6G by the more stable dye PDI for these measurements. The autocorrelation function $C'_r(t)$ (cf. Eq. 5) of the fluorescence anisotropy is calculated from polarized intensity time traces and fitted by a single exponential, which gives the rotation correlation time directly. The squares in Fig. 5 represent FACS measurements on PDI in glycerol when the temperature of the cryostat is varied between 190 and 240 K. These data, which closely follow the viscosity variation of glycerol, will be discussed in more detail in a forthcoming publication (R. Zondervan, J. Berkhout, F. Kulzer, and M. Orrit, unpublished data).

Here, we use FACS measurements for an independent temperature calibration of the hot spot between 200 and 220 K, obtained from anisotropy time traces of 100 s with 10-ms resolution. The cryostat temperature, 182 K, was chosen low enough to practically freeze out rotation on the experimental timescale in the absence of heating (cf. Fig. 5). Upon heating with variable power (between 0 and 4 mW), reorientations give rise to fluctuations of the anisotropy signal, whose correlation yields the rotation correlation time and hence the temperature at the center of the hot spot (cf. Eqs. 5 and 2). Fig. 9 *a* shows four autocorrelation functions with their single-exponential fits. Fig. 9 *b* displays the resulting calibration curve of the temperature in the center of the hot spot as a function of NIR power. The relation is linear with a slope of 10.3 K/mW (the heating is less efficient here because the metal film is pure Cr instead of NiCr). In this limited temperature window (200–240 K), the steep temperature dependence of the rotation time considerably improves

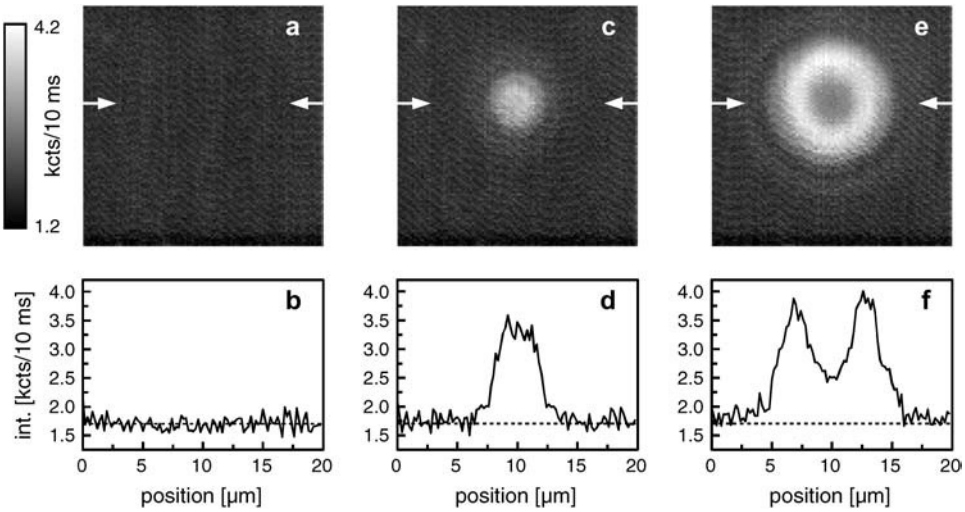

FIGURE 7 Intensity images. Confocal fluorescence images, 20 × 20 μm^2 of a glycerol film doped with R6G for NIR heating powers of 0 mW (*a*), 5 mW (*c*), or 8.5 mW (*e*). Graphs (*b*, *d*, and *f*) show the cross sections of images *a*, *c*, and *e* through the center of the heating spot. The total fluorescence images reveal the formation of a bright spot at first (*c*), then of a darker center surrounded by a bright and persistent ring (*e*).

the temperature determination over fluorescence anisotropy (cf. Fig. 5). The accuracy ($\pm\sigma$) becomes $\pm$0.5 K instead of $\pm$5 K.

Kinetics of heating and cooling

Here, we investigate the heating and cooling kinetics of the hot spot using fluorescence intensity and anisotropy of R6G in glycerol. To achieve a satisfactory signal/noise ratio with a time resolution of 1 μs, we chop the NIR intensity with an AOM and average the heating and cooling transients of many bright and dark periods, with a Picoquant (Berlin, Germany) TimeHarp 200 photon-counting card. To avoid spurious effects from long-term heating, we first determine the minimum cooling time required after each heating phase. Setting the cooling time to 100, 200, 500, or 1000 μs, with a constant heating time of 200 μs, and averaging the heating anisotropy transient for 100 ms at a NIR power of 11 mW, we find a constant anisotropy average of 0.14 for cooling times longer than 200 μs. We obtain a significantly lower value of 0.12 with the shorter cooling time of 100 μs. We therefore measure the kinetics with a square modulation of the NIR power at 2.5 kHz (200 μs heating followed by 200 μs cooling). The visible intensity is 50 W/cm^2, the NIR power is either 5.4, 7.0, or 11 mW, and the total observation time 600 s (1.5×10^6 periods).

Fig. 10 *a* shows the time-resolved total fluorescence (parallel and perpendicular channels added) in the center of the NIR focus for R6G in glycerol, during heating (first 200 μs with NIR power high) and cooling (second 200 μs with no NIR power). The total intensity gradually increases upon heating and reaches a higher final value for higher NIR power. Upon cooling, the intensity reverts to its initial value at a rate much higher than for heating. This pronounced asymmetry stems from the highly nonlinear dependence of intensity on temperature, complicated by the slow time response of photoblinking to temperature changes. The nonlinearity also manifests itself in the nonlinear dependence of

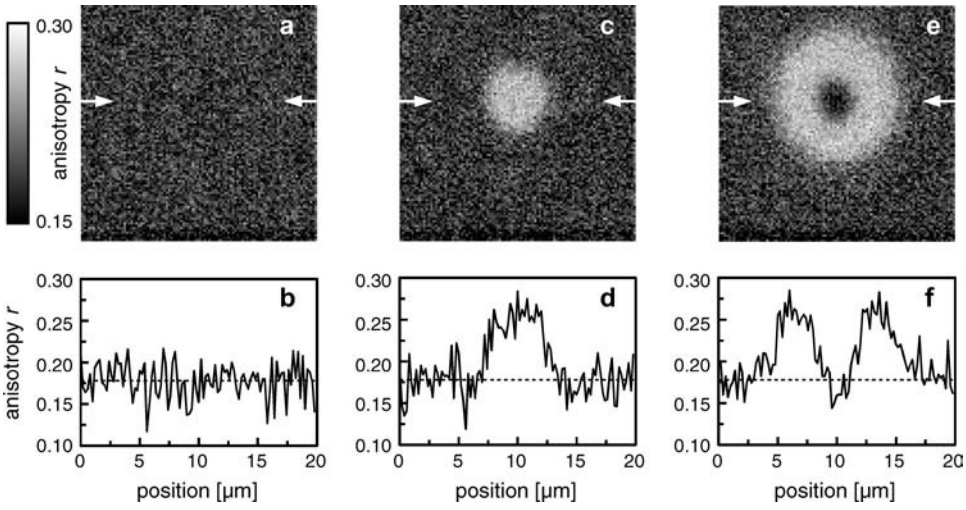

FIGURE 8 Anisotropy images. The data of Fig. 7 provide 20 × 20 μm^2 images of fluorescence anisotropy. Graphs (*b*, *d*, and *f*) show cross sections of images *a*, *c*, and *e* through the center of the heating spot. The images show first a high-anisotropy spot (*c*). Then, the anisotropy at the center decreases below the initial level, but is still above it in a (nonpersistent) ring (*e*). The temperature calibration curve of Fig. 6 gives the temperature in the center, 280 K for 5 mW (*c*) and 335 K for 8.5 mW (*e*).

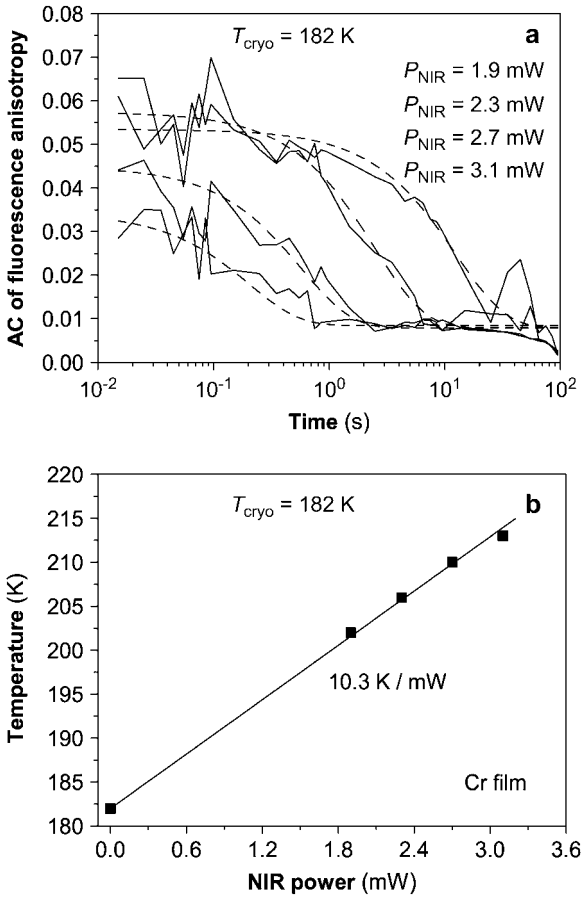

FIGURE 9 (*a*) Autocorrelation functions of the fluorescence anisotropy of PDI in glycerol at the center of the heating spot for NIR powers of 1.9, 2.3, 2.7, and 3.1 mW. The fluorescence anisotropy is recorded for 100 s with a time resolution of 10 ms. The dashed lines are fits to Eq. 5 yielding rotation correlation times of 12.5, 2.5, 0.58, and 0.20 s. (*b*) Calibration of the temperature at the hot spot's center with heating power. The dependence is again linear (*solid line*) with the somewhat weaker slope of 10.3 K/mW than in Fig. 6 because of the weaker absorption of the chromium film. The typical inaccuracy ($\pm 2\sigma$) of the fits in panel *a* is $\sim \pm 20\%$, but the steep temperature dependence of the rotational diffusion (cf. Fig. 5) leads to a very precise determination of temperature (accuracy of ± 0.5 K), about the size of the symbols.

fluorescence on heating power (compare the initial signal at 130 K with its maxima for 5.4, 7.0, and 11 mW).

The fluorescence anisotropy is expected to be less sensitive to photoblinking than the total intensity. Fig. 10 *b* shows anisotropy calculated from the same data. The initial anisotropy value, 0.132, is distinctly lower than 0.178, observed in the imaging experiments at 130 K (cf. Figs. 6 *a* and 8 *b*). This is probably a consequence of photoinduced processes (we remain for 600 s at the same sample position instead of 10 ms as in the imaging experiments). For 5.4 mW NIR power, the anisotropy variation due to heating is barely detectable. For the two higher heating powers, the variation appears clearly, but with an extreme asymmetry between apparent heating and cooling kinetics (the response to cooling appears much faster than to heating). This asymmetry obviously follows from the steady-state temperature variations of anisotropy (see Fig. 6 *a*). Upon heating, the initial anisotropy increase, due to photoblinking, is suppressed because the blinking kinetics are too slow to follow heating on a microsecond timescale (35). The drop in anisotropy due to molecular rotation at temperatures higher than 280 K, on the contrary, is very fast. Therefore, our fast anisotropy-based thermometer only works above 280 K, i.e., for high enough heating powers, and then only at the end of the heating period and at the beginning of the cooling period.

To convert the anisotropy plots into temperature traces, we can neglect photoblinking and only consider the effect of rotational diffusion described by Eq. 4; see solid curve in Fig. 6 *a*. Fig. 11 shows the temperature responses during heating and cooling for 7.0 and 11 mW, calculated from the data of Fig. 10 *b*. Below 280 K, the temperature cannot be determined and the plots are very noisy. Between 280 and 300 K the accuracy is low because of the large uncertainty in r_0. Above 300 K the accuracy in the temperature determination is $\pm 2\sigma = \pm 3$ K.

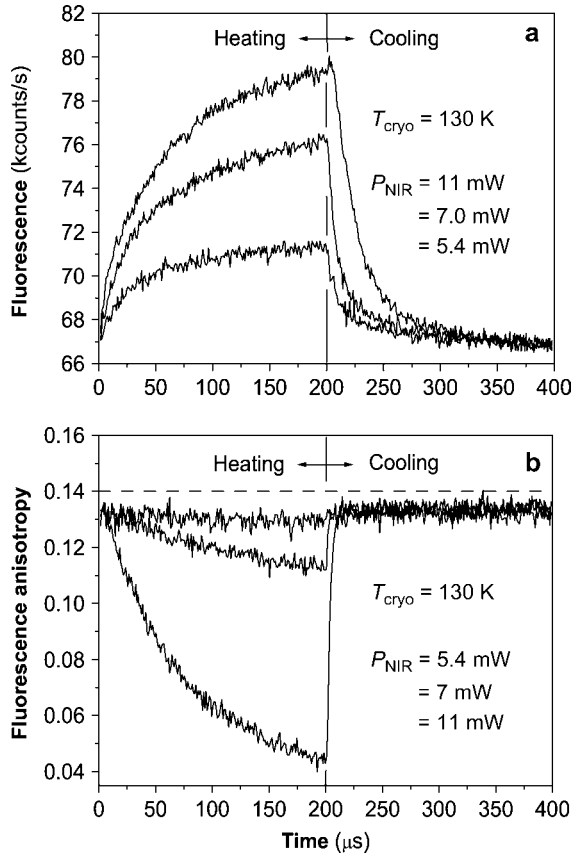

FIGURE 10 (*a*) Total fluorescence intensity response for R6G in glycerol at the center of the hot spot during heating (first 200 μs) and subsequent cooling (second 200 μs) at NIR powers of 5.4, 7.0, and 11 mW. The time resolution is 1 μs. (*b*) Simultaneous time dependence of the anisotropy, from the same data.

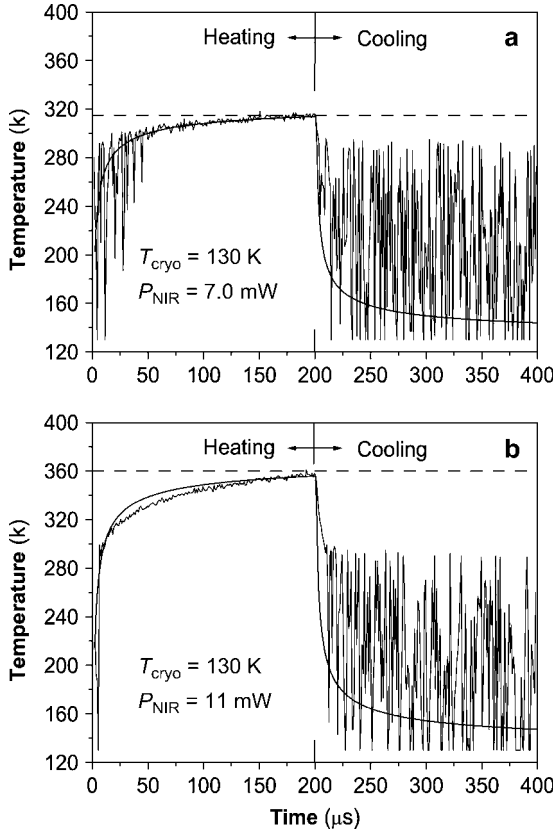

FIGURE 11 Temperature response during heating (first 200 μs) and cooling (second 200 μs) for NIR heating powers of 7.0 mW (*a*) and 11 mW (*b*). The plots are derived from the anisotropy traces in Fig. 10 *b*. The time resolution is 1 μs. The smooth lines are simulations of the temperature response according to the heat equation, cf. Eqs. 9 and 12. The fit of the data in panel *a* is nearly perfect, yielding a $t_{1/2}$ of ~3.5 μs. The deviation of the simulation in panel *b* is assigned to the different regime of heat transport in fluid glycerol above 310 K.

For discussion purposes, we characterize the heating and cooling kinetics by the time $t_{1/2}$ needed to reach half of the final temperature difference. To fit the experimental temperature traces of Fig. 11, we solve the heat equation (40) in an approximate way with a micrometer-sized point source heating the semiinfinite glass substrate (the heat diffusivity of glycerol is ~5× lower than that of glass (29)) at a constant power during $\tau_1 = 200$ μs, and turned off during the rest of the period (second 200 μs). The solution during the heating period is:

$$T(t) = T_{cryo} + A\left(\frac{1}{\sqrt{\tau_0}} - \frac{1}{\sqrt{t}}\right), \quad (9)$$

with $T_{cryo} = 130$ K and

$$\tau_0 = \frac{a^2}{6\kappa}, \quad (10)$$

where a is the radius of the initial heating spot and κ the thermal diffusivity of the heated medium (glass).

$$A = \frac{P}{2c(\pi\kappa)^{3/2}}, \quad (11)$$

with P the heating power and c the volume-specific heat of the hot spot. The solution during the cooling periods ($t > \tau_1$) is:

$$T(t) = T_{cryo} + A\left(\frac{1}{\sqrt{(t-\tau_1)}} - \frac{1}{\sqrt{t}}\right). \quad (12)$$

Excellent agreement to the curve at 7.0 mW (cf. Fig. 11 *a*) is obtained with $\tau_0 = 1$ μs and $A = 0.20$ Ks$^{1/2}$. The τ_0 value corresponds to a heating spot size of 3–4 μm, which is in good agreement with what we have observed in the imaging experiments. The value of A is 75% of the value obtained when literature values (39) for glass are inserted for c and κ and the absorption coefficient of the metal film is 30%. With the same parameters, we calculate the expected profile for 11 mW heating power. As shown in Fig. 11 *b*, there is a significant deviation from the experimental data. We attribute this to the change in transport properties of the glycerol film at temperatures higher than 300 K (see Fig. 6 *b*). From the theoretical curve at 7.0 mW, we can determine a $t_{1/2}$ value of 3.5 μs.

In the previous paragraph, we have established that temperature changes of up to 200 K are possible in a few microseconds. Reaching the equilibrium temperature within a few Kelvin may still take 150 μs. However, for an actual temperature-cycle experiment (cf. Fig. 1), the time resolution is only limited by the time it takes to reach T_{quench}, the temperature where the process of interest is frozen. If the cryostat temperature T_{cryo} is chosen such that $T_{quench} = (T_{cryo} + T_{high})/2$, this quenching time is $t_{1/2}$, i.e., a few microseconds. Let us illustrate this by the supercooling of water. The ice-formation rate is 3 K/μs for pure water but orders of magnitude less when cryoprotectants like glycerol or trehalose are added (41–43). When liquid water is cooled at this rate well past its freezing point, supercooled water is obtained. Let us take $T_{quench} = 260$ K. Under our current experimental conditions, $T_{cryo} = 130$ K, it would take less than a microsecond to reach 260 K from room temperature (295 K). The average freezing rate is ~50 K/μs, fast enough to supercool even pure water. The ability to supercool water is also of experimental interest because it means that large biomolecules, like DNA and proteins, can be reversibly temperature cycled. If the cooling were too slow, these molecules would be damaged by the expanding ice.

CONCLUSION

We have directly shown that local heating by a focused laser generates a micrometer-sized hot spot with temperature changes of several hundreds of Kelvin in a few microseconds. We have imaged the hot spot through the polarized fluorescence of a dye. This method has enabled us to calibrate the temperature between 200 and 350 K with an ac-

curacy ($\pm 2\sigma$) of ± 5 K. In this broad temperature range, various temperature-dependent processes can be used, e.g., reversible photoinduced processes (photoblinking), or rotational diffusion. In the limited temperature range 200–220 K, we could calibrate the temperature more accurately (± 0.5 K) by analyzing rotational diffusion through fluorescence anisotropy correlation spectroscopy. Owing to the fast response of rotational diffusion above 280 K, we have measured the high-temperature parts of the heating and cooling responses in real time. The heating and cooling are characterized by a half-time of ~ 4 μs. These results show the feasibility of temperature jumps of up to 200 K in ~ 1 μs.

The next step of this work will be to apply temperature cycles to study the dynamics of single molecules at room temperature. The dynamical process of interest will be decomposed into a series of freeze-measure-thaw evolution cycles, where the duration of the steps will be varied (cf. Fig. 1). Our method has three potential advantages over room-temperature single-molecule experiments: i), It will yield a longer observation time of each single molecule because the optical probing is performed at low temperature where photobleaching is considerably reduced (44); ii), Its time resolution does not depend on the fluorescence rate but is limited to the heating and cooling times. This will result in a time resolution of microseconds in the best cases. In a conventional single-molecule experiment, such a time resolution would require very high excitation intensities, which would dramatically reduce the observation time; iii), The local (high) temperature (cf. Fig. 1) can be quickly adjusted. This will significantly speed up mechanistic analysis, during which the temperature is varied to monitor the activation energies of different reaction pathways. The temperature-cycle experiment seems particularly promising for the single-molecule analysis of protein folding, a process extending over many timescales (45), and to follow repeated folding events of one and the same single protein.

We thank Elsbeth van der Togt and Joris Berkhout for their contributions to the experiments and Dr. Markus Lippitz for the development of the data acquisition software and his continuing support. We acknowledge the preparation of the initial metal films in our institute by M. B. S. Hesselberth in the group of Prof. J. Aarts.

This work is part of the research program of the ''Stichting voor Fundamenteel Onderzoek der Materie'' (FOM) and is financially supported by the ''Nederlandse Organisatie voor Wetenschappelijk Onderzoek'' (NWO). F.K. acknowledges a Marie Curie Fellowship from the European Commission (contract No. HPMF-CT-2001-01233).

REFERENCES

1. Phillips, C. M., Y. Mizutani, and R. M. Hochstrasser. 1995. Ultrafast thermally-induced unfolding of RNase-A. *Proc. Natl. Acad. Sci. USA.* 92:7292–7296.
2. Ballew, R. M., J. Sabelko, and M. Gruebele. 1996. Direct observation of fast protein folding: the initial collapse of apomyoglobin. *Proc. Natl. Acad. Sci. USA.* 93:5759–5764.
3. Munoz, V., P. A. Thompson, J. Hofrichter, and W. A. Eaton. 1997. Folding dynamics and mechanism of beta-hairpin formation. *Nature.* 390:196–199.
4. Callender, R. H., R. B. Dyer, R. Gilmanshin, and W. H. Woodruff. 1998. Fast events in protein folding: the time evolution of primary processes. *Annu. Rev. Phys. Chem.* 49:173–202.
5. Gruebele, M. 1999. The fast protein folding problem. *Annu. Rev. Phys. Chem.* 50:485–516.
6. Eaton, W. A., V. Munoz, S. J. Hagen, G. S. Jas, L. J. Lapidus, E. R. Henry, and J. Hofrichter. 2000. Fast kinetics and mechanisms in protein folding. *Annu. Rev. Biophys. Biomol. Struct.* 29:327–359.
7. Ansari, A., S. V. Kuznetsov, and Y. Q. Shen. 2001. Configurational diffusion down a folding funnel describes the dynamics of DNA hairpins. *Proc. Natl. Acad. Sci. USA.* 98:7771–7776.
8. Rabl, C. R., S. R. Martin, E. Neumann, and P. M. Bayley. 2002. Temperature jump kinetic study of the stability of apo-calmodulin. *Biophys. Chem.* 101:553–564.
9. Dimitriadis, G., A. Drysdale, J. K. Myers, P. Arora, S. E. Radford, T. G. Oas, and D. A. Smith. 2004. Microsecond folding dynamics of the F13WG29A mutant of the β-domain of staphylococcal protein a by laser-induced temperature jump. *Proc. Natl. Acad. Sci. USA.* 101:3809–3814.
10. Chung, H. S., M. Khalil, A. W. Smith, Z. Ganim, and A. Tokmakoff. 2005. Conformational changes during the nanosecond-to-millisecond unfolding of ubiquitin. *Proc. Natl. Acad. Sci. USA.* 102:612–617.
11. Denk, W., D. W. Piston, and W. W. Webb. 1995. Two-Photon Molecular Excitation in Laser Scanning Microscopy. Plenum, New York. 445–458.
12. Schönle, A., and S. W. Hell. 1998. Heating by absorption in the focus of an objective lens. *Opt. Lett.* 23:325–327.
13. Svoboda, K., and S. M. Block. 1994. Biological applications of optical forces. *Annu. Rev. Biophys. Biomol. Struct.* 23:247–285.
14. Liu, Y., D. K. Cheng, G. J. Sonek, M. W. Berns, C. F. Chapman, and B. J. Tromberg. 1995. Evidence for localized cell heating induced by infrared optical tweezers. *Biophys. J.* 68:2137–2144.
15. Peterman, E. J. G., F. Gittes, and C. F. Schmidt. 2003. Laser-induced heating in optical traps. *Biophys. J.* 84:1308–1316.
16. Segur, J. B., and H. E. Oberstar. 1951. Viscosity of glycerol and its aqueous solutions. *Ind. Eng. Chem.* 43:2117–2120.
17. Shankar, P. N., and M. Kumar. 1994. Experimental-determination of the kinematic viscosity of glycerol water mixtures. *Proc. R. Soc. Lond. A. Math. Phys. Eng. Sci.* 444:573–581.
18. Schröter, K., and E. Donth. 2000. Viscosity and shear response at the dynamic glass transition of glycerol. *J. Chem. Phys.* 113:9101–9108.
19. Blazhnov, I. V., N. P. Malomuzh, and S. V. Lishchuk. 2004. Temperature dependence of density, thermal expansion coefficient and shear viscosity of supercooled glycerol as a reflection of its structure. *J. Chem. Phys.* 121:6435–6441.
20. Enderlein, J., and C. Zander. 2002. Theoretical foundations of single molecule detection in solution. *In* Single Molecule Detection in Solution. Wiley-VCH Verlag, Berlin, Germany. 21–67.
21. Hess, S. T., and W. W. Webb. 2002. Focal volume optics and experimental artifacts in confocal fluorescence correlation spectroscopy. *Biophys. J.* 83:2300–2317.
22. Valeur, B. 2002. Molecular Fluorescence: Principles and Applications. Wiley-VCH Verlag, Berlin, Germany.
23. Aragon, S. R., and R. Pecora. 1975. Fluorescence correlation spectroscopy and Brownian rotational diffusion. *Biopolymers.* 14:119–137.
24. Mets, U. 2001. Fluorescence Correlation Spectroscopy: Theory and Applications. Springer-Verlag, New York.
25. Barcellona, M. L., S. Gammon, T. Hazlett, M. A. Digman, and E. Gratton. 2004. Polarized fluorescence correlation spectroscopy of DNA-DAPI complexes. *Microsc. Res. Tech.* 65:205–217.
26. Cathelinaud, M., F. Lemarquis, and C. Amra. 2002. Index determination of opaque and semitransparent metallic films: application to light absorbers. *Appl. Opt.* 41:2546–2554.

27. van der Meer, H., J. A. J. M. Disselhorst, J. Kohler, A. C. J. Brouwer, E. J. J. Groenen, and J. Schmidt. 1995. An insert for single-molecule magnetic-resonance spectroscopy in an external magnetic-field. *Rev. Sci. Instrum.* 66:4853–4856.

28. Bloess, A., Y. Durand, M. Matsushita, H. van der Meer, G. J. Brakenhoff, and J. Schmidt. 2002. Optical far-field microscopy of single molecules with 3.4 nm lateral resolution. *J. Microsc.* 205:76–85.

29. Sandberg, O., P. Andersson, and G. Backstrom. 1977. Heat-capacity and thermal-conductivity from pulsed wire probe measurements under pressure. *J. Phys.* [*E*]. 10:474–477.

30. Vogel, H. 1921. Temperature dependence of viscosity of melts. *Phys. Z.* 22:645.

31. Fulcher, G. S. 1925. Analysis of recent measurements of the viscosity of glasses. *J. Am. Ceram. Soc.* 8:339.

32. Tammann, G., and W. Hesse. Temperature dependence of viscosity of melted supercooled liquids. 1926. *Z. Anorg. Allg. Chem.* 156:245.

33. Dela Cruz, J. L., and G. J. Blanchard. 2002. The influence of chromophore structure on intermolecular interactions. A study of selected rhodamines in polar protic and aprotic solvents. *J. Phys. Chem. A.* 106:10718–10724.

34. Dempster, D. N., T. Morrow, and M. F. Quinn. 1973. The photochemical characteristics of rhodamine 6G-ethanol solutions. *J. Photochem.* 2:343–359.

35. Zondervan, R., F. Kulzer, S. B. Orlinskii, and M. Orrit. 2003. Photoblinking of rhodamine 6G in poly(vinyl alcohol): radical dark state formed through the triplet. *J. Phys. Chem. A.* 107:6770–6776.

36. Dibbernbrunelli, D., M. G. Deoliveira, and T. D. Z. Atvars. 1995. Temperature-dependence of the photobleaching process of fluorescein in poly(vinyl alcohol). *J. Photochem. Photobiol. A.* 85: 285–289.

37. Hou, Y. W., A. M. Bardo, C. Martinez, and D. A. Higgins. 2000. Characterization of molecular scale environments in polymer films by single molecule spectroscopy. *J. Phys. Chem. B.* 104:212–219.

38. Hou, Y. W., and D. A. Higgins. 2002. Single molecule studies of dynamics in polymer thin films and at surfaces: effect of ambient relative humidity. *J. Phys. Chem. B.* 106:10306–10315.

39. Weast, R. C., editor. 1968. Handbook of Chemistry and Physics, 49th Ed. CRC Press, Cleveland, OH.

40. Carslaw, H., and J. Jaeger. 1959. Conduction of Heat in Solids. Clarendon Press, Oxford, UK.

41. Angell, C. A., and Y. Choi. 1986. Crystallization and vitrification in aequous systems. *J. Microsc.* 141:251–261.

42. Sutton, R. L. 1991. Critical cooling rates to avoid ice crystallization in solutions of cryoprotective agents. *J. Chem. Soc. Faraday Trans.* 87: 101–105.

43. Branca, C., S. Magazu, G. Maisano, and P. Migliardo. 1999. Anomalous cryoprotective effectiveness of trehalose: Raman scattering evidences. *J. Chem. Phys.* 111:281–287.

44. Zondervan, R., F. Kulzer, M. A. Kol'chenko, and M. Orrit. 2004. Photobleaching of rhodamine 6G in poly(vinyl alcohol) at the ensemble and single-molecule levels. *J. Phys. Chem. A.* 108:1657–1665.

45. Dill, K. A., and H. S. Chan. 1997. From Levinthal to pathways to funnels. *Nat. Struct. Biol.* 4:10–19.